



Urea-bridging synthesis of nitrogen-doped carbon tube supported single metallic atoms as bifunctional oxygen electrocatalyst for zinc-air battery

Jing Zhao^a, Ruixuan Qin^b, Rui Liu^{a,*}

^a Ministry of Education Key Laboratory of Advanced Civil Engineering Materials, School of Materials Science and Engineering, and Institute for Advanced Study, Tongji University, Shanghai, 201804, China

^b Department of Chemistry, College of Chemistry and Chemical Engineering, Xiamen University, Xiamen, 361005, China



ARTICLE INFO

Keywords:

Urea
Carbon tube
Single atom
Bifunctional electrocatalyst
Zn-air battery

ABSTRACT

Single atom (SA) catalysts have recently emerged as promising candidates to substitute noble metals catalysts. Herein, a urea-bridge method has been exploited to fabricate stable metallic single atom dispersed on nitrogen-doped carbon tubes. The preparation involved a facile pyrolysis of ellagic acid (EA)-metal coordination compound mediated through the usage of urea. During the synthesis process, urea acted as a bridge to drive the formation of hollow carbon tube as well as to provide N sites to immobilize SA in a space-confined environment. The active SA sites together with the accessibility and rapid mass transport from the hollow substrate endowed the obtained EA-SAs (e.g. EA-Co-900, EA-Ni-900) outstanding performances in oxygen reduction/evolution reactions. Furthermore, EA-Co-900 showed a high power density (e.g. 73 mW cm⁻², at 65 mA cm⁻²) and excellent durability of 110 h at 20 mA cm⁻² when assembled into rechargeable zinc-air batteries.

1. Introduction

The development of sustainable energy conversion and storage technologies is crucial to mitigate the environmental and energy crisis. Metal-air battery has been identified as a promising energy storage device due to its high energy density, outstanding durability, security and low cost [1–4]. Efficient oxygen reduction (ORR) and evolution reactions (OER) bifunctional catalysts are urgently required for a rechargeable Zn-air battery, in which the kinetic is limited by the key discharge (ORR)/charge (OER) reactions taken place in the air-cathodes [5–7]. The foundational barriers are mainly coming from the high cost, scarcity along with poor durability of Pt and Ir or Ru-based benchmark catalysts for ORR and OER, respectively [8,9]. Therefore, the search for a low-cost, ultra-stable and highly efficient alternative catalyst is extremely urgent. Non-precious metals or their carbon nanocomposites have been emerging as one type of the most promising candidates to substitute noble metal catalysts toward rechargeable metal-air batteries [10,11]. Especially, metallic SA catalysts have represented the lowest size limit to achieve the maximum atom efficiency and expose the most active sites in catalysis. The unique electronic structure and unsaturated coordination environments of the active centers in SA catalyst have been proven to improve catalytic activity in a variety of electrocatalytic reactions [12–16].

Several strategies have been successfully developed to prepare a

series of SA catalysts, such as defect engineering, spatial confinement and coordination design [17–20]. For example, Bao et al. prepared atomically dispersed Cu(I)-N active sites in nitrogen-doped graphene by pyrolysis of copper phthalocyanine and dicyandiamide [21]. Wu et al. synthesized monodisperse Mn₄ active sites within porous three-dimensional carbon through leveraging the unique properties of zeolitic imidazolate frameworks (ZIF-8) [22]. To expose active sites and optimize catalytic kinetics, recent SA catalyst studies have been focused on exploring the substrates with desirable morphologies to stabilize isolated SAs as well as maximize their accessibility [23–25]. For example, Li et al. have prepared hollow carbon sphere to support Co SAs through SiO₂ template-assisted pyrolysis method [26]. They also fabricated a series of catalysts comprised of Fe SAs supported on hollow carbon polyhedron, which were directly pyrolyzed from a ZIF-8@poly(cyclo-triphosphazene-co-4,4'-sulfonyldiphenol) composite [13]. In the above-mentioned catalyst, the structural advantages from hollowness and porosity have strengthened the electronic control of atomically dispersed metal active sites, thereby facilitating sluggish catalytic kinetics and achieving excellent electrocatalytic performance.

Functional small molecules as bridging media have been widely used to precisely control the formation of different morphologies in organic or nanoscale self-assembly [27,28]. A wide variety of bridging groups, such as 4,4'-bipyridine, thiophene, urea and halogen ion, have been successfully demonstrated to tailor the functional assembled

* Corresponding author.

E-mail address: ruiliu@tongji.edu.cn (R. Liu).

materials through their flexible and diversified mediated ability [29–32]. For example, Shimizu et al. utilized urea bridging dibromide to synthesize small bis-urea macrocycles and then self-assembled into columnar tubes *via* intrinsic urea-urea hydrogen bonding [31]. Kolmer and the co-workers adopted fluorine as a programmed nanozipping to organize flexible oligophenylenes into a tailored nanographene on TiO₂ surfaces [32]. Inspired by the distinct functionality of bridging molecules in the assembled ensemble, here we developed a tailored urea-bridging strategy to construct isolated metal SAs anchored on N-doped hollow carbon tube (denoted as EA-SA). Starting from ellagic acid and M²⁺ (e.g. Co²⁺ or Ni²⁺), the assembled coordination EA-M nanosheets were successfully converted into EA-SA after pyrolysis under the bridging mediation of urea. The obtained EA-SA catalysts possessed atomically dispersed metallic SA sites for increasing the exposed active sites and hollow carbon tube for supporting the transport of relevant species in the catalytic process. The structural combination endowed EA-SAs excellent ORR/OER activity and higher performance than Pt/C + IrO₂ in Zn-air battery.

2. Experimental

2.1. Synthesis of EA-Co, EA-Co-900, EA-Co-T and EA-Co-900-R

Typically, 200 mg of ellagic acid (EA) were sufficiently dispersed in 15 mL of 0.1 M PBS (pH = 7.4). Then, 385 mg of Co(NO₃)₂·6H₂O were added in the suspension. Followed by sonication about 40 min, the mixture was hydrothermally treated at 100 °C for 24 h. EA-Co was collected by centrifugation, washed three times with deionized water and ethanol, respectively and dried 12 h under vacuum. 0.2 g of EA-Co and 0.45 g of urea (mass ratio of urea over EA-Co at 2.5) were fully grinded, then carbonized at 900 °C with a heating rate of 5 °C min⁻¹ under N₂ flow and followed by a HCl-leaching step to remove a few residual large Co crystals. The obtained sample was named EA-Co-900. EA-Co-T was prepared through the same procedure as that of EA-Co-900 except at the desired carbonization temperature (T). EA-Co-900-R was prepared *via* the same procedure as that of EA-Co-900 with the different feeding urea content (R represented mass ratio of urea/EA-Co).

2.2. Synthesis of EA-Ni, EA-Fe, EA-Ni-T, EA-Fe-900, EA-900 and EA-900-0

EA-Ni and EA-Fe were prepared through the same method as EA-Co except the usage of Ni(NO₃)₂·6H₂O or FeCl₂·4H₂O, respectively. 0.2 g of EA-Ni and 0.45 g of urea (mass ratio of urea over EA-Ni at 2.5) were sufficiently grinded, then carbonized at 900 °C with a heating rate of 5 °C min⁻¹ under N₂ flow and followed by a HCl-leaching step to obtain EA-Ni-900. EA-Ni-T was prepared from EA-Ni through the same procedure as that of EA-Ni-900 at the different carbonization temperature (T). EA-Fe-900 was prepared from EA-Fe *via* the similar carbonization condition as that of EA-Ni-900. 0.2 g of EA and 0.45 g of urea (mass ratio of urea over EA at 2.5) were sufficiently grinded, then carbonized at 900 °C with a heating rate of 5 °C min⁻¹ under N₂ flow to obtain EA-900. Directly carbonization of EA at 900 °C in the absence of urea led to the formation of EA-900-0.

2.3. Material characterizations

The structure and morphology of the synthesized materials were characterized by Transmission Electron Microscope (TEM, JEM-2100 F), JEM-ARM300 F (W_D) ED transmission electron microscope operating at 80 kV and X-ray Diffraction Spectrometry (XRD, D8 ADVANCE) with Cu Kα radiation (λ ¼ 1.5418 Å). X-ray photoelectron spectroscopy (XPS) was recorded on Axis Ultra DLD system using Al Kα radiation (1486.6 eV). XAFS spectra at the Co and Ni K-edge were collected at BL14W1 station in Shanghai Synchrotron Radiation Facility

(SSRF). The electron storage ring of SSRF was operated at 3.5 GeV with a maximum current of 250 mA. The Co and Ni K-edge XANES data were recorded in a fluorescence mode while Co and Ni foils were used as references, respectively. Fourier transform infrared (FTIR) spectra were collected from KBr pellets with a Nicolet NEXUS-470 FTIR spectrometer. Nitrogen adsorption-desorption isotherm was performed with a Quadrachrome adsorption instrument (Autosorb-iQ3; Quantachrome, America) at 77 K. The specific surface area was calculated by using the adsorption data *via* the Brunauer-Emmett-Teller (BET) method. The pore size distribution and the total pore volume were derived from the related adsorption branch by using the QSDFT model. Raman spectra were recorded on Horiba Lab RAM HR Evolution Raman spectrometer. Inductively coupled plasma atomic emission spectrometer (ICP-AES) analysis were conducted on an inductively coupled plasma atomic emission spectrometer (Optima 2100DV, US).

2.4. Electrochemical measurements

The electrochemical measurement was performed at room temperature through using a CHI-760e electrochemical analyzer with a three-electrode cell system. A glassy carbon electrode (0.196 cm², Pine Instrument Co., USA) loaded with the as-prepared sample used as the working electrode, whereas Pt and Ag/AgCl (3.5 M KCl) were served as counter and reference electrode during the measurement, respectively. The catalyst ink was obtained by sonicating 5 mg of sample or commercial Pt/C (20 wt. % Pt) in a mixture of 0.65 mL of ethanol and 15 μL of Nafion (5%).

The ORR measurement was conducted in O₂-saturated 0.1 M KOH solution. The loading of the sample and Pt/C on the working electrode was 0.36 mg cm⁻² and 0.10 mg cm⁻² in O₂-saturated 0.1 M KOH, respectively. The CV and LSV test were conducted at a scan rate of 10 mV s⁻¹. All potentials in this study were converted against the reversible hydrogen electrode (RHE). The number of electrons transferred per oxygen molecule involved in the ORR was analyzed on the basis of the Koutecky-Levich equations:

$$\frac{1}{J} = \frac{1}{J_K} + \frac{1}{J_L} = \frac{1}{J_K} + \frac{1}{B\omega^{1/2}} \quad (1)$$

$$B = 0.2nFD_0^{2/3}\nu^{-1/6}C_O \quad (2)$$

here, *J* represents the measured current density, whereas *J_K* and *J_L* mean the kinetic and diffusion limiting current density, respectively; *ω* stands for the electrode revolution rate, *n* represents the transferred electron number in ORR process; *F* is the Faraday constant (F = 96,485 C/mol), *D_O* represents the oxygen molecular diffusion coefficient in 0.1 M KOH (1.9×10^{-5} cm²/s), *ν* is the kinematic viscosity of the electrolyte (1.009×10^{-2} cm²/s), *C_O* is a symbol of saturated O₂ concentration in the electrolyte (1.2×10^{-6} mol/cm³).

OER performance of the obtained catalysts was estimated from LSV in 1 M KOH at a scan rate of 5 mV s⁻¹ with the total catalyst loading of 0.36 mg cm⁻². Tafel slopes were calculated based on the Tafel equation:

$$\eta = b \log(j) + a \quad (3)$$

Where *η*, *j* and *b* are the over potential, measured current density and Tafel slope, respectively.

Zn-air batteries were performed in a laboratory-constructed electrochemical cell. A carbon paper electrode (3.14 cm²) loaded with 10 mg of EA-Co-900, EA-Ni-900 or Pt/C + IrO₂ was served as cathode and Zn foil was served as anode. 6 M KOH filled with 0.2 M Zn(Ac)₂ was applied as electrolyte. The discharge polarization and power density plots were recorded by using a galvanodynamic method. Galvanostatic discharge-charge cycling curve was conducted at room temperature, in which one cycle consisted of one discharge step followed by one charge step of the same current density and duration time (20 mA cm⁻² for 100 h with a 10 min cycling).

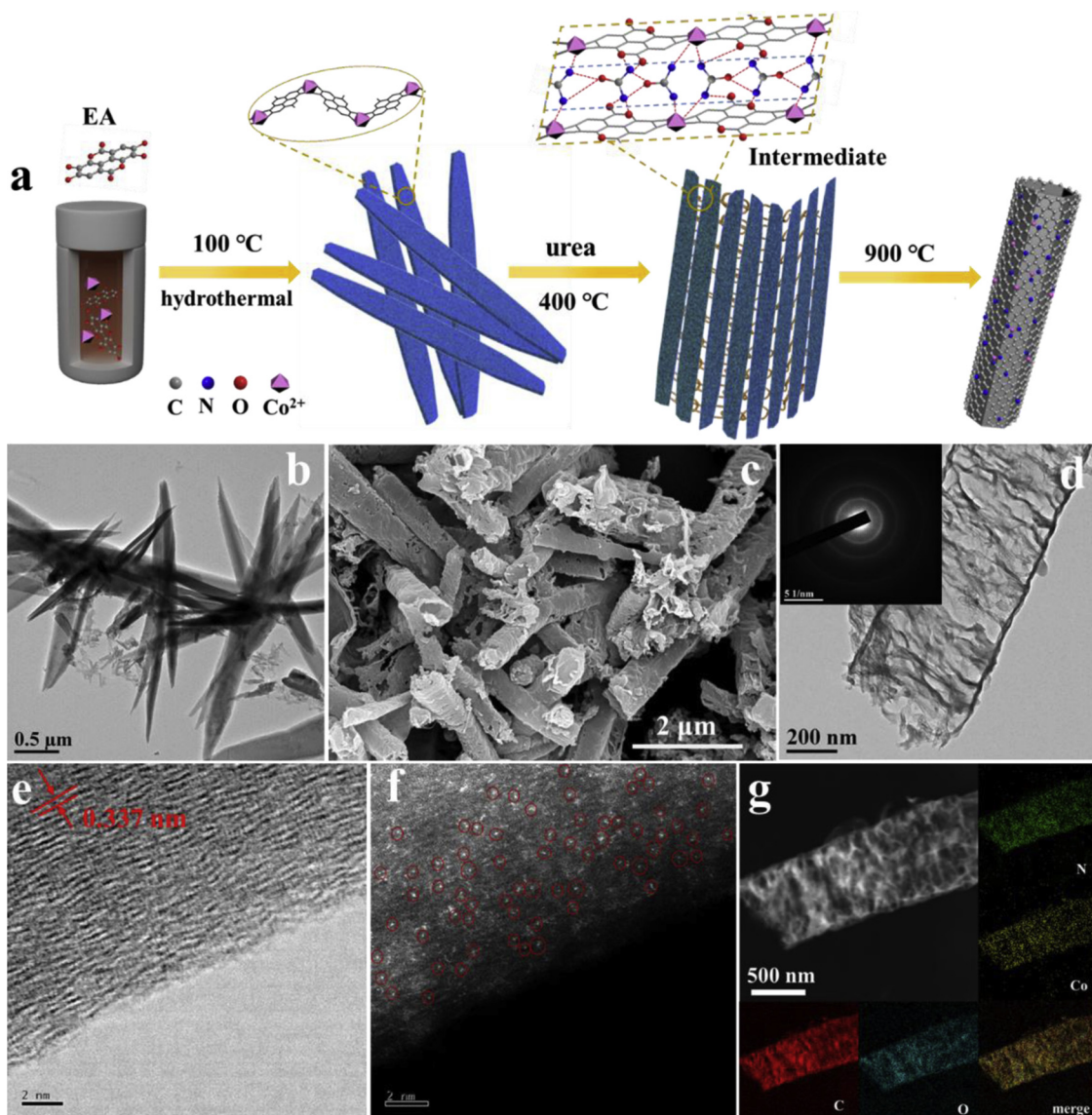


Fig. 1. (a) Schematic illustration of the synthesis of EA-Co-900. (b) TEM image of EA-Co. (c) SEM, (d)TEM (inset: corresponding SAED pattern), (e) Aberration-corrected BF-STEM, (f) HAADF- transition metals through its abundant STEM images and (g) corresponding EDX element mapping of EA-Co-900.

3. Results and discussion

3.1. Synthesis, structure and composition of materials

The synthesis process for N-doped carbon tubes supported Co SAs was schematically represented in Fig. 1a. Coordination of Co²⁺ and ellagic acid (EA) resulted in the formation of two-dimensional EA-Co nanosheets. Follow-up pyrolysis in the presence of urea led to the formation of Co SAs on nitrogen-doped hollow carbon tube (denoted as EA-Co-900). Polyphenolic acid, such as tannic acid, ellagic acid and gallic acid, has exhibited a strong metal coordination ability through its catechol/pyrogallol groups [33–35]. In our synthesis, the hydrothermal treatment of EA and Co²⁺ first led to the formation of a coordination nanosheet (EA-Co) with a bamboo leaf-like morphology and mono-dispersed length around approximately 3–5 μm (SEM and TEM images in Fig. S1a and Fig. 1b, respectively). The coordination between EA and Co ion was also demonstrated through the vanishing of characteristic O–H vibration peaks of EA in Fourier transform infrared (FT-IR) spectra (Fig. S2) [34]. Then, carbonization of EA-Co in the presence of urea to 900 °C drove the nanosheets assembled into hollow tube with an average diameter of 600 nm (EA-Co-900 in Fig. 1c and d). The

corresponding ring-like selected area electron diffraction (SAED) pattern of an individual tube illustrated its poor crystallinity (Fig. 1d inset). To illuminate the form of Co SAs, we performed aberration corrected BF-STEM and HAADF-STEM measurement with subangstrom resolution. The heavier isolated Co atoms and few small clusters could be lightly discerned in the graphitized carbon support and labelled with red circles in Fig. 1e and f and Fig. S1c. The scanning transmission electron microscopy (STEM) with elemental mapping in Fig. 1g clearly revealed that Co, N, and C were homogeneously distributed over the whole carbon tube. A few residual Co crystals were also observed and dispersed in a carbon nanofilm (Fig. S1b), which might be resulted from the fact that the EA-Co nanosheets un-involved in the tube formation were unable to impede the migration of Co atoms and hence resulted in the formation of Co nanoparticles [36]. The high-resolution N 1s XPS spectrum in Fig. 2a implied that the dominant N species in EA-Co-900 were pyridinic-N and graphitic-N, which could serve as anchor points for Co SAs. The binding energy of the Co 2p_{3/2} signal locating at 780.02 eV (Fig. 2b) indicated that the valence of Co was between Co⁰ and Co²⁺ owing to a slight positive charge resulting from N coordination [37]. Furthermore, the Co K-edge X-ray absorption near-edge structure (XANES) spectra of EA-Co-900 and the reference Co foil

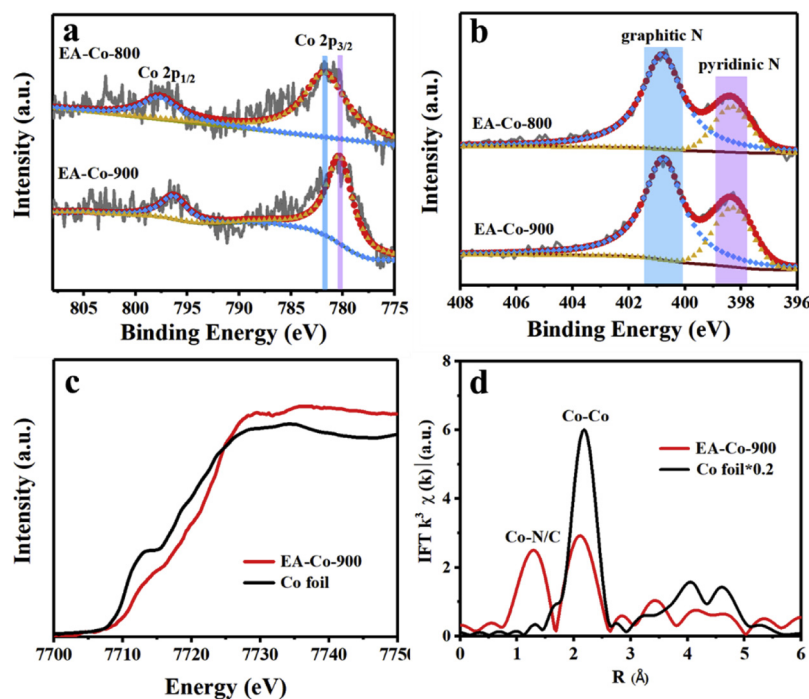


Fig. 2. (a) High resolution XPS spectra for N 1s, (b) XPS spectra for the Co 2p regions of EA-Co-800 and EA-Co-900. (c) XANES spectra at the Co K-edge, (d) Fourier transform (FT) at the Co K-edge of EA-Co-900 and Co foil.

were presented in Fig. 2c. The peak position of EA-Co-900 was located more positive than that of Co foil, indicating that the valence state of Co atom was situated higher than Co⁰. The Fourier transform (FT) k^3 -weighted $\chi(k)$ function of the extended X-ray absorption fine structure (EXAFS) spectrum for EA-Co-900 showed the peak at 1.27 Å, which belonged to the first coordination shell of Co-N/C (Fig. 2d). The peak at 2.13 Å indicated the existence of small Co clusters in EA-Co-900, which was in agreement with the above TEM result [26,27,38]. The loading amount of Co in EA-Co-900 was 2.17 wt %, as determined by ICP-AES.

The morphological evolution during the pyrolysis of EA-Co was monitored to trace the formation process and illustrated in Fig. 3. The EA-Co nanosheets connected together at 400 °C and commenced the formation of bamboo slip-like ensemble in the presence of urea. These conjoined nanosheets formed a hollow tube when the temperature increased to 500 °C as the thermally driven process might bend thin layers and roll-up into tube [39]. Simultaneously, EA-Co decomposed initially at 500 °C and converted to N-doped carbon as suggested in the X-ray diffraction (XRD) patterns (Fig. S3). Further raising the temperature made the framework of hollow tube nanostructure transparent and meanwhile, the degree of graphitization gradually enhanced with the increase of carbonization degree (Fig. S3 and S4). As shown in the corresponding SAED patterns, the degree of crystallinity gradually decreased and accompanied by the disappearance of Co particles due to the thermodynamically stable coordination of metal atom with N under high temperature (insets in Fig. 3) [40]. The binding energy of the Co 2p_{3/2} signal (Fig. 2b) was down-shifted from 782.16 to 780.02 eV along with the carbonization temperature rising from 800 to 900 °C, which further manifested a slight positive charge of Co in EA-Co-900. N₂ sorption isotherms illustrated the existence of both micropore and mesopore in all EA-Co-T samples. The calculated Brunauer – Emmett – Teller (BET) surface areas increased with the carbonization temperature, up to 268 m² g⁻¹ for EA-Co-900 (Fig. S5 and Table S1).

Two control experiments were carried out to study the effect of urea and metal ion on the formation of EA-SAs. First, we synthesized EA-Co-900-R with different feeding urea content (R represented mass ratio of urea over EA-Co). TEM in Fig. S6 showed that abundant Co

nanostructures were dispersed on the carbon film in EA-Co-900-0 and EA-Co-900-1. When the urea/EA-Co mass ratio increased to 2.5 or 3, hollow tube with SAs were formed. Furthermore, a bunch of larger Co nanoparticles were observed in EA-Co-900-8. The comparison illustrated the role of urea in the formation of tube as well as SAs. At a lower urea content, insufficient molecular bridges and N sites were unable to completely link EA-Co nanosheets and stabilize Co SAs. The ratio ranged from 2.5 to 3 well matched the dual function abilities of urea in nanosheet connection and SA stabilization. The higher urea content could lead to the formation of two-dimensional C₃N₄, which hindered the growth of tube (Fig. S7) and in turn demonstrated the beneficial effect of space-confined tube on the formation of SAs [41]. Another control experiment was performed by carbonization of both EA and EA-urea in the absence of Co²⁺. Neither EA-900-0 nor EA-900 possessed the morphology of hollow tube along with a low specific surface area (Fig. S8 and S9), illustrating the node functionality of the coordinated Co²⁺ in the construction of skeleton. Hence, we envision the following formation process of EA-Co-900 in Fig. 1a: during the carbonization process, urea molecules served as tailored bridges to connect EA-Co nanosheets and further drive them into hollow tube. At the same time, Co SAs were achieved via the coexistence of N sites and space-confinement from tube formation.

The urea-assisted bridging strategy was further tested for fabricating other EA-SA materials. EA and Ni was coordinated into EA-Ni, followed by carbonization into EA-Ni-900 in the presence of urea (Fig. S10). Single Ni atoms were readily tracked in the substrate with the even distribution of Ni, N and C over the whole tube (Fig. 4b-d). The original EA-Ni nanosheets were successfully transformed into hollow carbon tube with poor crystallinity (Figs. 4a and S11). The heavier isolated Ni XPS results manifested both pyridinic-N and graphitic-N as well as the ionic Ni^{δ+} ($0 < \delta < 2$) nature of Ni (Fig. S12) [42]. XANES spectra (Fig. 4e) showed the intensity of EA-Ni-900 located higher than that of Ni foil. The FT k^3 -weighted $\chi(k)$ function of EXAFS spectrum exhibited Ni – N coordination with a peak at 1.31 Å (Fig. 4f) [42,43]. Additionally, the peak at 2.11 Å revealed the existence of small Ni clusters in EA-Ni-900. The content of Ni in EA-Ni-900 was determined by ICP-AES analysis to be approximately 3.04 wt %. EA-Ni-900 possessed

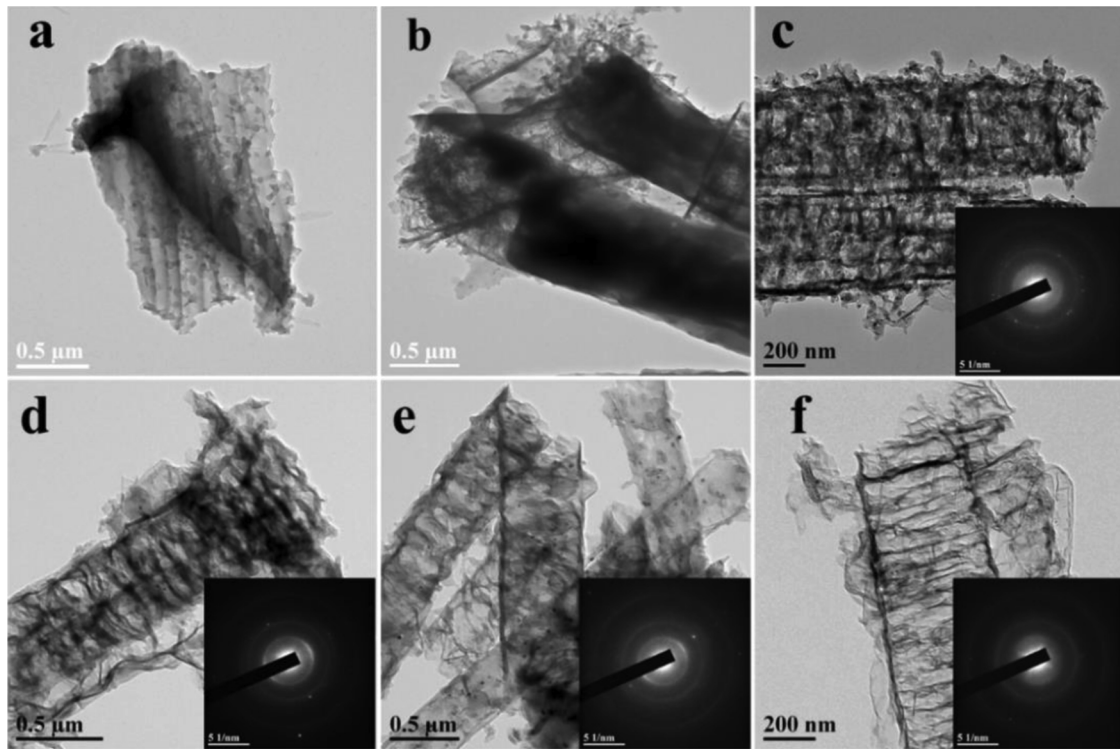


Fig. 3. TEM images of (a) EA-Co-400, (b) EA-Co-500, (c) EA-Co-600, (d) EA-Co-700, (e) EA-Co-800 and (f) EA-Co-900. (inset: corresponding SAED patterns).

similar growth process as that of EA-Co-900 (Fig. S13-S16). Different from EA-Co and EA-Ni, EA-Fe particle from EA and Fe^{2+} coordination possessed bulky morphology (Fig. S17a and S18a,b). In our previous report, EA and Fe^{3+} also coordinated into amorphous particles [44]. We ascribe the failure of designed nanosheet in EA-Fe system to the undefined coordination environment from transitional oxygen states between Fe^{2+} and Fe^{3+} . As illustrated in Fig. S17b, trivalent iron might destroy the environment of orientational coordination and thus formed amorphous bulky particles. As a result, Fe and Fe_3C particles deposited on N-doped carbon film was produced in EA-Fe-900 (Fig. S18c,d, S19 and S20).

3.2. Electrochemical characterization of catalysts

The electrocatalytic activity for ORR was investigated in a three-electrode system with a rotating disk electrode, using O_2 -saturated 0.1 M KOH as the electrolyte. ORR peak potential E_p in the cyclic voltammetry (CV) (Fig. S21a) and half-wave potential $E_{1/2}$ in linear sweep voltammetry (LSV) curve (Fig. 5a) indicated that EA-Co-900 ($E_p = 0.85$ V; $E_{1/2} = 0.84$ V) and EA-Ni-900 ($E_p = 0.79$ V; $E_{1/2} = 0.78$ V) were higher than that of EA-900 ($E_p = 0.72$ V; $E_{1/2} = 0.75$ V) and commercial Pt/C ($E_p = 0.86$ V; $E_{1/2} = 0.82$ V). Furthermore, EA-Co-900 could achieve a higher diffusion-limited current density (5.6 mA cm^{-2})

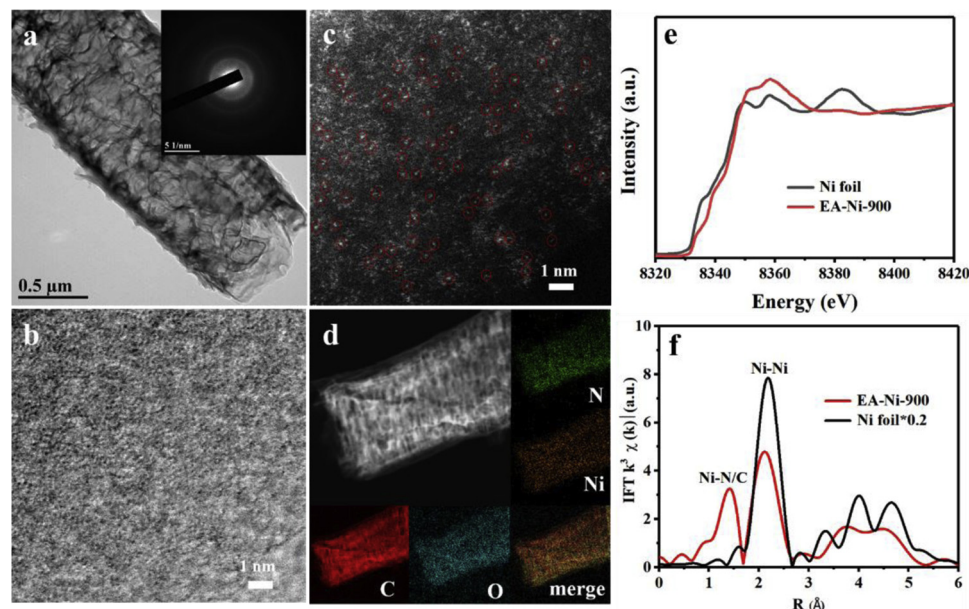


Fig. 4. (a) TEM (inset: corresponding SAED pattern). (b) Aberration-corrected BF-STEM. (c) HAADF-STEM image and (d) corresponding element maps of EA-Ni-900. (e) XANES spectra at the Ni K-edge and (f) Fourier transform (FT) at the Ni K-edge of EA-Ni-900 and Ni foil.

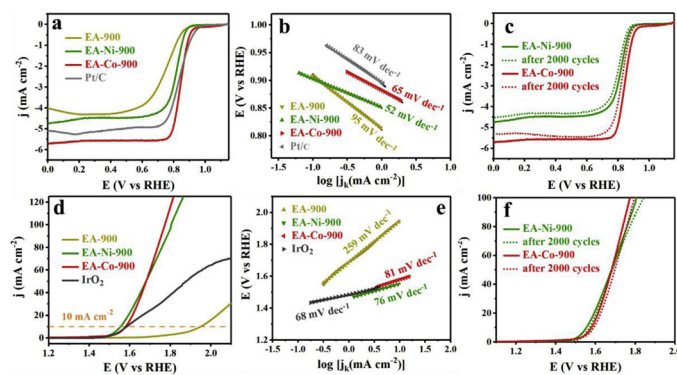


Fig. 5. (a) ORR polarization curves and (b) corresponding tafel plots of EA-900, EA-Co-900, EA-Ni-900 and Pt/C. (c) Durability test of the EA-Co-900 and EA-Ni-900 catalysts for 2000 cycles in O₂-saturated 0.1 M KOH. (d) OER polarization curves and (e) corresponding tafel plots of EA-900, EA-Co-900, EA-Ni-900 and IrO₂. (f) Durability test of the EA-Co-900 and EA-Ni-900 catalysts for 2000 cycles in O₂-saturated 1 M KOH.

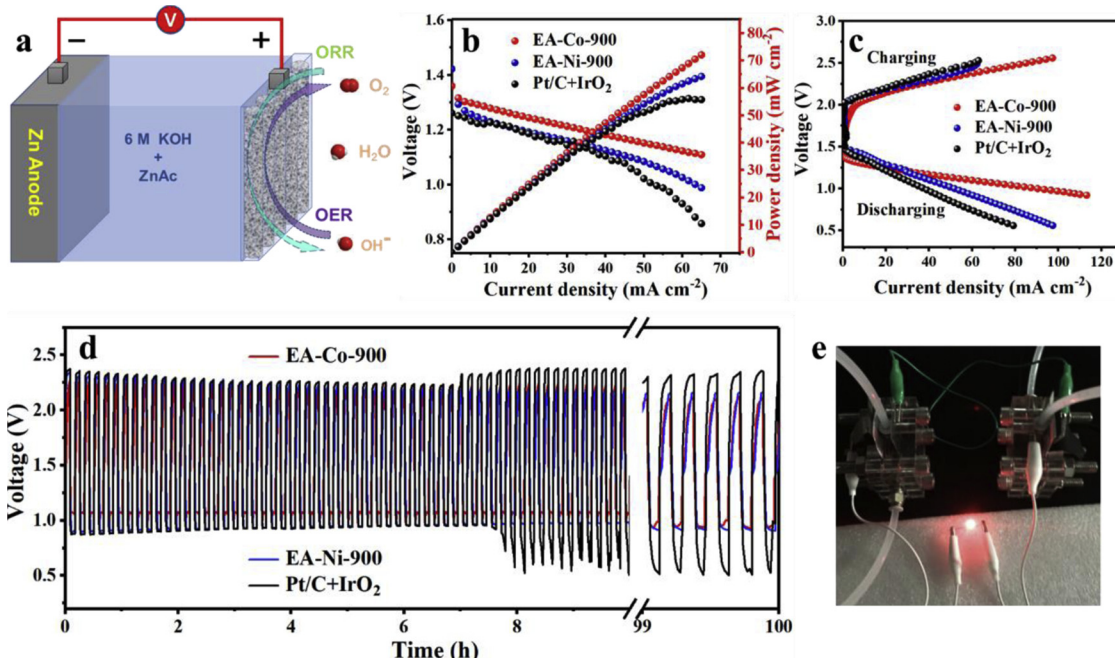


Fig. 6. (a) Schematic representation of the Zn-air battery. (b) Polarization and power density curves of Zn-air batteries and (c) charge and discharge polarization curves with EA-Co-900, EA-Ni-900 and Pt/C + IrO₂. (d) Galvanostatic discharge-charge cycling curves at 20 mA cm⁻² of rechargeable Zn-air batteries with EA-Co-900, EA-Ni-900 and Pt/C + IrO₂ on carbon paper, respectively. (e) A lighted red LED (~ 3 V) powered by two integrated Zn – air batteries interconnected in series (For interpretation of the references to colour in this figure legend, the reader is referred to the web version of this article).

than that of Pt/C (5.5 mA cm⁻²). [45–47] The higher performance of EA-SAs than that of EA-900 evidently illustrated the critical role of highly dispersed Co or Ni SAs as well as small clusters in the ORR process. Meanwhile, EA-Co-900 and EA-Ni-900 performed comparably to both 20 wt% Pt/C and the best reported Co/Ni-based ORR electrocatalysts (Table S2). In addition, EA-Co-900 and EA-Ni-900 also exhibited more positive LSV among the series of EA-Co-T and EA-Ni-T samples, respectively (Fig. S21b and S22a). These results further revealed that the active catalytic sites were mainly derived from Co and Ni SAs. Both EA-Co-900 and EA-Ni-900 followed an almost-four-electron transfer pathway for catalyzing ORR based on the calculated results of K – L equation, reflecting the superior selectivity of direct O₂ reduction to OH⁻ (Fig. S21c,d and S22b-d) [6]. The smaller Tafel slope (65 mV dec⁻¹ for EA-Co-900, 51 mV dec⁻¹ for EA-Ni-900 vs 83 mV dec⁻¹ for 20 wt% Pt/C) in Fig. 6b further confirmed the outstanding ORR activity of EA-SAs. Moreover, EA-Co-900 and EA-Ni-900 showed excellent stability for ORR, as testified by the few absence of the LSV curves shift after 2000 CV cycles (Fig. 5c).

Regarding the OER activity (Fig. 5d), EA-Co-900 and EA-Ni-900 delivered current densities of 10.0 mA cm⁻² ($E_{j=10}$) at 1.57 and 1.55 V_{RHE}, smaller than that of the benchmark catalyst IrO₂ (1.58 V) and EA-900 (1.95 V). In Fig. 5e, the outstanding OER performance was further

certified through the Tafel slope of EA-Co-900 (81 mV dec⁻¹) and EA-Ni-900 (76 mV dec⁻¹) for a fast kinetic process when compared to EA-900 (259 mV dec⁻¹), and even close to IrO₂ (68 mV dec⁻¹). Similarly, both EA-Co-900 and EA-Ni-900 exhibited a higher OER activity among the samples of EA-Co-T and EA-Ni-T, respectively (Fig. S23). Importantly, both EA-Co-900 and EA-Ni-900 showed outstanding overall electrode activity as indicated by lower value ($\Delta E = 0.72$ V and 0.73 V for EA-Co-900 and EA-Ni-900, respectively) of the difference between the ORR and OER metrics ($\Delta E = E_{j10} - E_{1/2}$), outperforming most of the reported highly active reversible oxygen catalysts (Table S2). Besides, there were almost no decay in the OER polarization curves of EA-Co-900 and EA-Ni-900 after 2000 CV cycles, implying their high catalytic stability toward OER (Fig. 5f). It was believed that the outstanding performances for EA-SAs were mainly owing to their merits in structure and composition. Firstly, abundant active sites of SAs, small clusters and doped N in carbon framework enhanced ORR and OER activities. Then, the intrinsic hierarchical porosity along with the large surface area and good conductivity were beneficial for the permeation and diffusion of oxygen and liquid electrolyte as well as electron transfer during ORR/OER process. Furthermore, the hollow structure of tubes brought the catalysts fully contacting with the electrolyte, to the max exposing active sites along with strengthening catalytic kinetics [13].

In order to explore the catalysis potential of SAs, we firstly evaluated the catalytic performance of EA-Co-900-R, which presented with different Co existing forms (e.g. single atom, crystal, or mixed materials). As shown in Fig. S24, EA-Co-900 and EA-Co-900-3 with SAs and a few small crystal active sites showed both higher ORR and OER activity than other crystal dominated samples (EA-Co-900-0, EA-Co-900-1 and EA-Co-900-8), suggesting that SAs were necessary for the high ORR and OER activity of EA-Co-900. Additionally, the poisoning experiment was performed *via* using SCN⁻ to block the Co-N sites to explore its role in catalyzing ORR and OER [48]. Considering the instability of SCN⁻ ions in KOH solution, the catalytic activity was conducted in 0.1 M HClO₄ containing 0.01 M KSCN. Polarization curves in Fig. S25 showed that the ORR activity of EA-Co-900 decreased evidently in the presence of SCN⁻, and the OER activity of EA-Co-900 was also weakening. This result further illustrated that Co-N active sites could be an important role for ORR and OER activity.

3.3. Zn-air cell test

To evaluate the utility of EA-SAs in a practical device, a primary Zn-air battery was assembled (Fig. 6a). The open-circuit potential of EA-Co-900 based Zn-air battery was 1.37 V (Fig. S26a). The polarization and power density curves in Fig. 6b indicated that the EA-Co-900 cathode indicated a peak power density of 73 mW cm⁻², which was 18 mW cm⁻² higher than that of Pt/C + IrO₂ (55 mW cm⁻²) at the same current density. The discharge/charge polarization curves in Fig. 6c illustrated that the voltage gap between charge and discharge of EA-Co-900 was lower than that of Pt/C + IrO₂, implying its better rechargeability [49]. Furthermore, the EA-Co-900 based battery revealed an excellent cycling stability at the constant current density of 20 mA cm⁻² for 100 h (Fig. 6d). The excellent durability of EA-Co-900 also could be demonstrated through the continuous lighting of a light emitting diode (LED) pattern (-3 V) by two integrated Zn-air batteries in series for over 24 h without no obvious brightness decay (Fig. 6e and Fig. S26b). As illustrated in Fig. 6b-d, the EA-Ni-900 based Zn-air battery also possessed an outperforming performance than that of Pt/C + IrO₂.

4. Conclusion

In summary, a general strategy enabling the controlled synthesis of hollow carbon tube supported metallic single atoms has been developed. In the pyrolysis process of EA-metal coordination nanosheet, the addition of urea serving as a tailored molecule bridge could construct the hollow carbon nanotube with the coexistence of N doping and space-confined SAs. The unique features of the well dispersed single active sites along the hierarchical hollow tube could bestow the obtained EA-Co-900 and EA-Ni-900 excellent performances in ORR/OER and Zn-air battery. This finding may open up a facile synthetic approach in the preparation of single-atomic metal materials for catalysis and energy conversion.

Notes

The authors declare no competing financial interest.

Acknowledgements

We thank the Shanghai Synchrotron Radiation Facility for providing beamline time and for supporting our XAS analysis. We would like to acknowledge Shanghai Municipal Natural Science Foundation (No. 17ZR1432200), National Natural Science Foundation of China (No. 21774095), the start-up funding from Tongji University and the Young Thousand Talented Program.

Appendix B. Supplementary data

Supplementary material related to this article can be found, in the online version, at doi:<https://doi.org/10.1016/j.apcatb.2019.117778>.

References

- [1] Q. Wang, Y. Ji, Y. Lei, Y. Wang, Y. Li, S. Wang, ACS Energy Lett. 3 (2018) 1183–1191.
- [2] J. Ying, G. Jiang, Z.P. Cano, Z. Ma, C. Zhong, D. Su, Z. Chen, Appl. Catal. B-Environ. 225 (2018) 496–503.
- [3] X. Zhu, T. Jin, C. Tian, C. Lu, X. Liu, M. Zeng, X. Zhuang, S. Yang, L. He, H. Liu, S. Dai, Adv. Mater. 29 (2017) 1704091.
- [4] Q. Wang, Y. Lei, Z. Chen, N. Wu, Y. Wang, B. Wang, Y. Wang, J. Mater. Chem. A Mater. Energy Sustain. 6 (2018) 516–526.
- [5] J.M. Qian, X.S. Guo, T.T. Wang, P.T. Liu, H. Zhang, D.Q. Gao, Appl. Catal. B-Environ. 250 (2019) 71–77.
- [6] L. An, Z.Y. Zhang, R.B. Gupta, P.X. Xi, S. Zhang, J. Am. Chem. Soc. 140 (2018) 17624–17631.
- [7] J. Zhao, C. Li, R. Liu, Nanoscale 10 (2018) 5882–5887.
- [8] Q. Liu, Y. Wang, L. Dai, J. Yao, Adv. Mater. 28 (2016) 3000–3006.
- [9] L. Chong, J. Wen, J. Kubal, F.G. Sen, J. Zou, J. Greeley, M. Chan, H. Barkholtz, W. Ding, D.-J. Liu, Science 362 (2018) 1276–1282.
- [10] H.H. Jin, H. Zhou, D.P. He, Z.H. Wang, Q.L. Wu, Q.R. Liang, S.L. Liu, S.C. Mu, Appl. Catal. B-Environ. 250 (2019) 143–149.
- [11] Z. Chen, Q. Wang, X. Zhang, Y. Lei, W. Hu, Y. Luo, Y. Wang, Sci. Bull. (Beijing) 63 (2018) 548–555.
- [12] Y. Zheng, Y. Jiao, Y.H. Zhu, Q. Cai, A. Vasileff, L.H. Li, Y. Han, Y. Chen, S.Z. Qiao, J. Am. Chem. Soc. 139 (2017) 3336–3339.
- [13] Y. Chen, S. Ji, A.I. Rykov, S. Cai, H. Tang, Z. Zhuang, C. Chen, Q. Peng, D. Wang, Y. Li, Nat. Commun. 9 (2018) 5422.
- [14] C. Zhu, Q. Shi, B.Z. Xu, D. Du, S.P. Beckman, D. Su, Y. Lin, Adv. Energy Mater. 8 (2018) 1801956.
- [15] T. Sun, L. Xu, D. Wang, Y. Li, Nano Res. (2019), <https://doi.org/10.1007/s12274-019-2345-4>.
- [16] H.T. Chung, D.A. Cullen, D. Higgins, B.T. Sneed, E.F. Holby, K.L. More, P. Zelenay, Science 357 (2017) 479–484.
- [17] Y. Chen, S. Ji, C. Chen, Q. Peng, D. Wang, Y. Li, Joule 2 (2018) 1242–1264.
- [18] H. Zhang, G. Liu, L. Shi, J. Ye, Adv. Energy Mater. 8 (2018) 1701343.
- [19] B. Qiao, A. Wang, X. Yang, L.F. Allard, Z. Jiang, Y. Cui, J. Liu, J. Li, T. Zhang, Nat. Chem. 3 (2011) 634.
- [20] X. Wang, W. Wang, M. Qiao, G. Wu, W. Chen, T. Yuan, Q. Xu, M. Chen, Y. Zhang, X. Wang, J. Wang, J. Ge, X. Hong, Y. Li, Y. Wu, Y. Li, Sci. Bull. (Beijing) 63 (2018) 1246–1253.
- [21] H. Wu, H. Li, X. Zhao, Q. Liu, J. Wang, J. Xiao, S. Xie, R. Si, F. Yang, S. Miao, X. Guo, G. Wang, X. Bao, Energy Environ. Sci. 9 (2016) 3736–3745.
- [22] J. Li, D.A. Cullen, G.E. Sterbinsky, Z. Feng, D. Su, K.L. More, G. Wang, Z. Wang, G. Wu, Nat. Catal. 1 (2018) 935–945.
- [23] D.H. Guo, R. Shibuya, C. Akiba, S. Saji, T. Kondo, J. Nakamura, Science 351 (2016) 361–365.
- [24] K. Strickland, E. Miner, Q.Y. Jia, U. Tylus, N. Ramaswamy, W.T. Liang, M.T. Sougrati, F. Jaouen, S. Mukerjee, Nat. Commun. 6 (2015) 7343.
- [25] J. Liang, R.F. Zhou, X.M. Chen, Y.H. Tang, S.Z. Qiao, Adv. Mater. 26 (2014) 6074–6079.
- [26] Y. Han, Y.G. Wang, D. Wang, Y. Li, J. Am. Chem. Soc. 139 (2017) 17269–17272.
- [27] S. Dawn, M.B. Dewal, D. Sobrangsingh, P.J. Pellechia, L.S. Shimizu, J. Am. Chem. Soc. 133 (2011) 7025–7032.
- [28] C.R. Bowers, M. Dvoyashkin, S.R. Salpage, C. Akel, H. Bhase, M.F. Geer, L.S. Shimizu, ACS Nano 9 (2015) 6343–6353.
- [29] F.E. Hahn, C. Radloff, T. Pape, A. Hepp, Organometallics 27 (2008) 6408–6410.
- [30] E.B. Cho, D. Kim, M. Jaroniec, Langmuir 23 (2007) 11844–11849.
- [31] L.S. Shimizu, A.D. Hughes, K.D. Shimizu, J. Am. Chem. Soc. 125 (2003) 14972–14973.
- [32] M. Kolmer, R. Zuzak, S. Godlewski, M. Szymonski, K. Amsharov, Science 363 (2019) 57–60.
- [33] P. Zhang, L. Wang, P.F. Fulvio, M.F. Chisholm, S. Dai, Nat. Commun. 8 (2017) 15020.
- [34] S.J. Yang, M. Antonietti, N. Fechler, J. Am. Chem. Soc. 137 (2015) 8269–8273.
- [35] P.F. Zhang, H.Y. Li, G.M. Veith, S. Dai, Adv. Mater. 27 (2015) 234–239.
- [36] J. Wei, Y. Liang, Y. Hu, B. Kong, J. Zhang, Q. Gu, Y. Tong, X. Wang, S.P. Jiang, H. Wang, Angew. Chem. Int. Ed. 55 (2016) 12470–12474.
- [37] P. Yin, T. Yao, Y. Wu, X. Hong, Z. Deng, G. Zhou, S. Wei, Y. Li, Angew. Chem. Int. Ed. 55 (2016) 10800–10805.
- [38] X. Wang, Z. Chen, X. Zhao, T. Yao, W. Chen, R. You, C. Zhao, G. Wu, J. Wang, W. Huang, J. Yang, X. Hong, S. Wei, Y. Wu, Y. Li, Angew. Chem. Int. Ed. 57 (2018) 1944–1948.
- [39] S. Iijima, Nature 354 (1991) 56.
- [40] S. Wei, A. Li, J.C. Liu, Q. Peng, L. Gu, X. Han, J. Li, Y. Li, Nat. Nano. 13 (2018) 856–861.
- [41] M.L. Zhang, Y.G. Wang, W.X. Chen, J.C. Dong, L.R. Zheng, J. Luo, J.W. Wan, S.B. Tian, W.C. Cheong, D.S. Wang, Y.D. Li, J. Am. Chem. Soc. 139 (2017) 10976–10979.
- [42] C. Zhao, X. Dai, T. Yao, S. Wei, Y. Wu, Y. Li, J. Am. Chem. Soc. 139 (2017) 8078–8081.

[43] C. Zhao, X. Wang, J. Wang, J. Luo, Y. Li, H. Duan, Y. Wu, Y. Li, Joule 3 (2019) 1–11.

[44] J. Zhao, N. Fu, R. Liu, ACS Appl. Mater. Inter. 10 (2018) 28509–28516.

[45] M. Shao, Q. Chang, J.-P. Dodelet, R. Chenitz, Chem. Rev. 116 (2016) 3594–3657.

[46] X. Wang, Z. Li, Y. Qu, T. Yuan, W. Wang, Y. Wu, Y. Li, Chem. (2019), <https://doi.org/10.1016/j.chempr.2019.03.002>.

[47] M. Liu, Z. Zhao, X. Duan, Y. Huang, Adv. Mater. 31 (2019) 1802234.

[48] H. Luo, W.-J. Jiang, C. Lin, W. Dong, S. Niu, L.-B. Huang, X. Zhang, Z. Wei, J.-S. Hu, Chem. Commun. (Camb.) 54 (2018) 8190–8193.

[49] C. Li, M. Wu, R. Liu, Appl. Catal B-Environ. 244 (2019) 150–158.